



HAL
open science

Effect of Isovalent Substitution on the Electronic Structure and Thermoelectric Properties of the Solid Solution $\alpha\text{-As}_2\text{Te}_3\text{-xSex}$ ($0 \leq x \leq 1.5$)

Jean-Baptiste Vaney, Gaëlle Delaizir, Bartłomiej Wiendlocha, Janusz Tobola, Eric Alleno, Andrea Piarristeguy, Antonio P. Goncalves, Christine Gendarme, Bernard Malaman, Anne Dauscher, et al.

► To cite this version:

Jean-Baptiste Vaney, Gaëlle Delaizir, Bartłomiej Wiendlocha, Janusz Tobola, Eric Alleno, et al.. Effect of Isovalent Substitution on the Electronic Structure and Thermoelectric Properties of the Solid Solution $\alpha\text{-As}_2\text{Te}_3\text{-xSex}$ ($0 \leq x \leq 1.5$). *Inorganic Chemistry*, 2017, 56, pp.2248–2257. 10.1021/acs.inorgchem.6b02930 . hal-01475939

HAL Id: hal-01475939

<https://hal.science/hal-01475939>

Submitted on 9 Mar 2023

HAL is a multi-disciplinary open access archive for the deposit and dissemination of scientific research documents, whether they are published or not. The documents may come from teaching and research institutions in France or abroad, or from public or private research centers.

L'archive ouverte pluridisciplinaire **HAL**, est destinée au dépôt et à la diffusion de documents scientifiques de niveau recherche, publiés ou non, émanant des établissements d'enseignement et de recherche français ou étrangers, des laboratoires publics ou privés.

**Effect of Isovalent Substitution on the Electronic Structure and Thermoelectric
Properties of the Solid Solution α -As₂Te_{3-x}Se_x ($0 \leq x \leq 1.5$)**

Jean-Baptiste Vaney^{1,+}, Gaëlle Delaizir², Bartłomiej Wiendlocha³, Janusz Tobola³, Eric
Alleno⁴, Andrea Piarristeguy⁵, Antonio Pereira Gonçalves⁶, Christine Gendarme¹, Bernard
Malaman¹, Anne Dauscher¹, Christophe Candolfi¹, Bertrand Lenoir^{1*}

¹ *Institut Jean Lamour (IJL), UMR 7198 CNRS-Université de Lorraine, Nancy, France*

² *Sciences des Procédés Céramique et de Traitement de Surface (SPCTS), UMR CNRS 7315-
Université de Limoges, Limoges, France*

³ *AGH University of Science and Technology, Faculty of Physics and Applied Computer
Science, Al. Mickiewicza 30, 30-059 Krakow, Poland*

⁴ *Institut de Chimie et des Matériaux Paris Est (ICMPE), UMR 7182 CNRS-Université Paris-
Est Créteil, Thiais, France*

⁵ *Institut Charles Gerhardt (ICG), UMR 5253 CNRS-Université de Montpellier, Montpellier,
France*

⁶ *C2TN, Instituto Superior Técnico, Universidade de Lisboa, P-2695-066 Bobadela, Portugal*

Abstract

We report on the influence of Se substitution on the electronic band structure and thermoelectric properties (5 – 523 K) of the solid solution $\alpha\text{-As}_2\text{Te}_{3-x}\text{Se}_x$ ($0 \leq x \leq 1.5$). All the polycrystalline compounds $\alpha\text{-As}_2\text{Te}_{3-x}\text{Se}_x$ crystallize isostructurally in the monoclinic space group $C2/m$ (no. 12, $Z = 4$). Regardless of the Se content, chemical analyses performed by scanning electron microscopy and electron probe microanalysis indicate a good chemical homogeneity, with only minute amounts of secondary phases for some compositions. In agreement with electronic band structure calculations, neutron powder diffraction suggests that Se does not randomly substitute for Te but exhibits a site preference. These theoretical calculations further predict a monotonic increase in the band gap energy with the Se content, which is confirmed experimentally by absorption spectroscopy measurements. Increasing x up to $x = 1.5$ leaves unchanged both the p -type character and semiconducting nature of $\alpha\text{-As}_2\text{Te}_3$. The electrical resistivity and thermopower gradually increase with x as a result of the progressive increase in the band gap energy. Despite $\alpha\text{-As}_2\text{Te}_3$ exhibits very low lattice thermal conductivity κ_L , the substitution of Se for Te further lowers κ_L down to $0.35 \text{ W m}^{-1} \text{ K}^{-1}$ at 300 K. The compositional dependence of the lattice thermal conductivity closely follows classical models of phonon alloy scattering, indicating that this decrease is due to enhanced point-defect scattering.

Introduction

Thermoelectric materials are attracting attention due to their ability to convert a temperature gradient into an electrical potential (Seebeck effect) and vice-versa (Peltier effect). These reciprocal effects potentially pave the way to versatile technologies that include waste-heat harvesting devices and cooling set-ups. The thermoelectric performances of a material are evaluated by its dimensionless thermoelectric figure of merit ZT defined as $ZT = \alpha^2 T / \rho \kappa$, where α , ρ , κ and T stand for the thermopower (or Seebeck coefficient), the electrical resistivity, the total thermal conductivity, and the absolute temperature, respectively.^{1,2} Achieving high ZT values in a broad temperature range is however very challenging due to the subtle balance between the electronic and thermal properties that must be obtained.^{1,2}

For thermoelectric applications near room temperature, the rhombohedral Bi_2Te_3 and its derivatives of general chemical formula Pn_2Ch_3 ($\text{Pn} = \text{Bi}, \text{Sb}$ and $\text{Ch} = \text{Te}, \text{Se}, \text{S}$; space group $R\bar{3}m$) have been considered as canonical compounds for several decades^{1,2} and still remain one of the most studied families of thermoelectric materials nowadays.³⁻⁶ In addition to reaching ZT values around unity near 300 K, either n -type or p -type semiconducting properties can be obtained, both of which being required for the fabrication of thermoelectric devices.^{1,2}

Despite being another isostructural member of this family, the binary $\beta\text{-As}_2\text{Te}_3$ has received less attention.⁷⁻⁹ The polymorphic compound As_2Te_3 exhibits a rich temperature-pressure phase diagram with several crystal structures identified recently.¹⁰⁻¹³ Under ambient pressure, this compound also crystallizes within a monoclinic structure ($\alpha\text{-As}_2\text{Te}_3$) with space group $C2/m$ (Figure 1).¹⁴⁻¹⁶ Both structures have recently drawn attention for their interesting thermoelectric properties originating from a favorable combination of semiconducting-like

electronic properties and particularly low lattice thermal conductivities (around $0.5 \text{ W m}^{-1} \text{ K}^{-1}$ at 300 K).^{17,18} Our investigations on the transport properties of α - and β -As₂Te₃ have unveiled the important role of charged defects akin to Bi₂Te₃-based alloys. In α -As₂Te₃, this defect chemistry yields either *n*- or *p*-type samples with carrier concentrations of the order of 10^{17} cm^{-3} depending on the synthesis conditions.¹⁷ Optimization of the thermoelectric properties could be realized in both compounds by tuning the electronic properties via substitutions of either Sn or Bi for As.^{17,19} These experimental studies have evidenced interesting *ZT* values of 0.65 at 423 K and 0.85 at 523K in *p*-type Sn-doped β -As₂Te₃ and α -As₂Te₃, respectively.^{17,18}

In the Bi₂Te_{3-x}Se_x solid solution, the Se/Te ratio controls the nature and the concentration of charged defects and thus, offers a control parameter to tune both the carrier concentration and the dominant carrier type.²⁰⁻²³ In order to determine whether a similar behavior emerges in α -As₂Te₃, we explore herein the influence of Se on the electronic structure and transport properties in a wide range of temperatures (5 – 523 K) of the solid solution α -As₂Te_{3-x}Se_x ($0 \leq x \leq 1.5$). In agreement with first-principles calculations, we show that increasing the Se content leads to an increase in the band gap energy and hence, to higher electrical resistivity values. Although the lattice thermal conductivity of α -As₂Te₃ is intrinsically very low, the formation of a solid solution results in even lower values that reach $0.35 \text{ W m}^{-1} \text{ K}^{-1}$ above 300 K due to enhanced point-defect scattering.

Experimental and computational details

Warning: At high temperatures, the As vapor pressure may be high enough to damage the quartz tube and release toxic As vapor.

Synthesis. All manipulations of solids and powders were carried out in a dry, argon-filled glove box with O₂ and H₂O contents of less than 0.1 ppm. Because the α form of the binary

As_2Se_3 is stable only at high pressure (under ambient pressure, As_2Se_3 crystallizes in the $P2_1/n$ space group) and due to the high electrical resistivity of the samples with high Se contents, the compositional range probed herein was restricted to $0 \leq x \leq 1.5$.^{24,25} Polycrystalline samples of $\alpha\text{-As}_2\text{Te}_{3-x}\text{Se}_x$ with $x = 0.0, 0.1, 0.2, 0.4, 0.7, 1.0$ and 1.5 were synthesized by direct reaction of stoichiometric amounts of pure As (Goodfellow, 99.99%), Te (5N+, 99.999%) and Se (5N+, 99.999%) in quartz tubes sealed under secondary vacuum. The sealed tubes were heated in a vertical furnace up to 923 K with a heating rate of approximately 10 K min^{-1} , dwelt at this temperature for 2 h and eventually furnace-cooled. Contrary to the synthesis of $\alpha\text{-As}_{2-x}\text{Sn}_x\text{Te}_3$ samples which requires an annealing treatment of the rhombohedral β -phase initially obtained after water quenching, the α phase has been here directly obtained by air quenching. It is worth noting that in the $\alpha\text{-As}_2\text{Te}_{3-x}\text{Se}_x$ system for $x \geq 0.1$, water quenching induces the formation of a glassy phase so that a single-phase material cannot be obtained. An additional annealing step at 573 K for 3 days has been further applied to improve the chemical homogeneity of the samples and suppress an eventual glassy phase. After a final quenching, the ingots were ground into micron-sized powders and consolidated by spark plasma sintering (SPS, Dr. Sinter 505 Syntex) between 553 and 593 K (the sintering temperature depending on the composition) under a pressure of 50 MPa for 2 min using a graphite die of 10.4 mm inner diameter. Due to the shrinkage of the sintering window with increasing x , the relative densities, determined by dimensions and weight of the cylindrical pellets, decrease from 98% ($x = 0.0$) to 93% ($x = 1.5$).

X-ray and Neutron Powder Diffraction. Phase purity and crystal structure were verified by X-ray powder diffraction (XRPD) with a Bruker D8 Advance diffractometer (Cu $K\alpha_1$ radiation) in reflection mode. Room-temperature neutron powder diffraction (NPD) patterns were collected on the $x = 0.7$ sample at the Institut Laue Langevin (ILL, Grenoble, France) on the high-resolution two-axis diffractometer D1B equipped with a one-dimensional curved

multidetector. Rietveld analyses of XRPD and NPD patterns were carried out using the Fullprof software.²⁶ Note that the layered crystal structure of these samples results in a slight renormalization of the intensities of the X-ray diffraction peaks, the extent of which varying from sample to sample.

Scanning Electron Microscopy and Electron Probe Microanalysis. Scanning electron microscopy (SEM) observations were conducted on polished bulk pieces using a Quanta FEG (650F, FEI) to probe the phase purity of the samples. Images of the surface were collected in the backscattering electron mode (BSE). Corresponding elemental X-ray mappings were performed to assess the chemical homogeneity of the samples.

Electron probe microanalysis (EPMA) was performed with a JEOL JXA 8530F equipped with wavelength-dispersive spectrometers. Prior to analyses, bulk pieces of the consolidated samples were carefully polished with alumina powders. Backscattered electrons were used for imaging the surface of the samples and contrast the matrix from possible secondary phases. In order to minimize matrix effects, X-ray intensities of As and Te were compared with those of a calibrated β -As₂Te₃ standard for quantitative analysis. The calibration of this sample was carried out with the isostructural compound Bi₂Te₃ as in our previous study on the α -As_{2-x}Sn_xTe₃ samples.¹⁷ The chemical compositions of the α -As₂Te_{3-x}Se_x specimens were determined by averaging the results obtained on at least 90 different points for each sample. Because of the good correlation between the actual and nominal Se contents, the latter will be used hereafter to label the samples.

Low- and high-temperature transport properties measurements. The dense cylindrical pellets were cut both parallel and perpendicular to the pressing direction with a diamond-wire saw to probe the anisotropy. Bar-shaped samples ($\sim 3 \times 2.5 \times 8$ mm³) were used to measure simultaneously the thermopower, the electrical resistivity and the thermal conductivity between 5 and 300 K using the thermal transport option (TTO) of a physical property

measurement system (PPMS, Quantum Design). For these measurements, four copper leads were brazed onto the surface of the samples with a low-melting-point braze. The same samples were used to determine the Hall resistivity from measurements of the transverse electrical resistivity using the AC transport option of the PPMS. These measurements were realized in a five-probe configuration under magnetic fields ranging between -1 T and $+1$ T. Due to the high electrical resistance of the samples for $x \geq 0.7$, the Hall coefficient could be only reliably obtained for $x \leq 0.4$. Furthermore, the semiconducting nature of the samples results in a rapid rise in the electrical resistivity upon cooling. For this reason, the transverse resistivity could be measured only in a narrow temperature range below 300 K.

Another set of bar-shaped samples (typical dimensions $\sim 1.5 \times 1.5 \times 8$ mm³) was cut in the two directions to measure the electrical resistivity and thermopower between 300 and 523 K. These two transport coefficients were measured simultaneously with a ZEM-3 apparatus (Ulvac-Riko). Thermal conductivity was determined from 300 up to 523 K via thermal diffusivity measurements performed on disk-shaped samples (~ 10 mm in diameter) for the parallel direction and on rectangular prism-shaped ($\sim 6 \times 6 \times 1$ mm³) samples for the perpendicular direction using a laser flash system LFA 467 (Netzsch). Prior to measurements, the samples were spray-coated with a thin layer of graphite to ensure a homogeneous signal absorption and emission on the respective surfaces. The thermal diffusivity a is related to the thermal conductivity by the relation $\kappa = aC_p\rho_v$ where C_p is the specific heat at constant pressure and ρ_v is the density. Specific heat measurements (DSC 403 F3, Netzsch) were carried out on the binary sample α -As₂Te₃ in the same temperature range by the continuous scanning method under argon flow, according to the ASTM E 1269 method. This sample was used as a reference sample for the specific heat measurements of the other samples using a LFA 467 Netzsch according to the ASTM E 1461-07 method. The combined uncertainty in the determination of the ZT values is estimated to be $\sim 17\%$ above 300 K.²⁷

Optical absorption. Optical absorption spectra were measured on disk-shaped samples at 300 K using a Thermo Scientific Nicolet 6700 FTIR spectrophotometer equipped with an integrated sphere. The electronic band gaps E_g were determined by applying the Kubelka-Munk theory that relates the measured reflectance R to a value proportional to the absorption coefficient $F(R) = (1 - R)^2/2R$.²⁸

Electronic Band Structure Calculations. Calculations of the electronic band structure of the series α -As₂Te_{3-x}Se_x ($x = 0.5, 1.0$ and 1.5) were carried out by the Korringa-Kohn-Rostoker (KKR) method with the coherent potential approximation (CPA) to treat explicitly the chemical disorder that accompanies the substitution of Se for Te.^{29,30} The exchange-correlation effects were taken into account using the Perdew-Wang formula in the local density approximation (LDA).³¹ Within this formalism, the fully charge self-consistent crystal potentials were constructed in the muffin-tin form. The position of the Fermi level was determined accurately by the generalized Lloyd formula.³² For all compositions, we used the experimental lattice parameters and atomic coordinates, as determined by Rietveld refinements of the XRPD patterns. For converged crystal potentials and atomic charges (convergence better than 1 mRy and $10^{-3}e$, respectively), total-, site- and orbital l -decomposed densities of states (DOS) were determined using a tetrahedron method for integration in the reciprocal k -space.³² Insights into the site preference of Se were obtained by total energy KKR-CPA calculations with Se selectively diluted on the three inequivalent Te sites of the crystal structure of α -As₂Te₃ (see Figure 1).

Results and Discussion

Electronic band structure calculations. Figure 2 shows the electronic DOS of α -As₂Te_{2.5}Se_{0.5} that illustrates the effect of Se selectively diluted on the three possible Te sites.

As can be expected, the isovalent substitution of Se for Te does not modify significantly the DOS and the energy gap at the Fermi level for all investigated compositions. This gap stems from a strong hybridization of the p -states of As and Te/Se. Inspecting in more details the site-decomposed DOS (Figures 2 to 4), the p -states of Se lie generally at higher energies in the upper part of the valence bands compared to the p -states of substituted Te, regardless on which Te site Se was placed. Remarkably, the overall DOS shape of Se2 is less structured than that of Se1 and Se3, both of which exhibiting more pronounced peaks just below the energy gap. Further, the center of gravity of Se2 DOS is shifted towards lower energies due to the larger DOS hump seen around -3eV below E_F with respect to the DOS of Se1 and Se3. All these features suggest that Se preferentially occupies the Te2 site. This conclusion, based on DOS characteristics, is well supported by the total energy KKR-CPA calculations, which clearly show that the lowest energy is obtained when Se occupies the Te2 site followed by the Te3 site and eventually the Te1 site. Interestingly, the energy difference of about 0.18 eV per atom between the first and the second case is much larger than the corresponding value between the second and third case (0.04 eV per atom, with a numerical accuracy of $\sim 0.1\text{ meV}$). This large difference further indicates a strong preference for Se to substitute on the Te2 site. Hence, in view of the KKR-CPA results, one can expect that Se should primarily replace Te2 with increasing the Se content up to the entire filling of this site, that is, up to $x = 1$. Indeed, similar comparison of total energy calculations performed for $\alpha\text{-As}_2\text{Te}_2\text{Se}$ shows that the energy difference between the case where Se fully substitutes Te either on the Te2 or Te3 site is about 0.5 eV per atom, a value much larger than in the above-mentioned composition ($x = 0.5$). The electronic reason for such trends can be also seen from DOS features by comparing the KKR-CPA results for $x = 1.0$ and 1.5 shown in Figures 3 and 4. The DOS peak of Se3 is almost twice larger than that of Se2 in the upper part of the valence states. Once the Te2 site is entirely filled by Se, the simultaneous presence of Se on both the

Te1 and Te3 sites represents the most unfavorable situation from an energetic point of view. Thus, for $x > 1.0$, Se should substitute on the Te3 site rather than Te1. This filling sequence is confirmed by the DOS of the $x = 1.5$ composition for which the difference in energy between these two cases is about 0.1 eV per atom in favor of Te3.

Another interesting finding derived from these calculations is related to the evolution of the energy gap with x . It should be kept in mind that the KKR-CPA computations were performed in the framework of the LDA approach, which tends to underestimate the energy gap. Thus, only the relative variations in the energy gap are meaningful, not the absolute values. This effect, inherent to the methodology used here, explains the discrepancy between the band gap energy calculated for the pristine compound As_2Te_3 in the present study ($E_g = 0.19$ eV) and the value obtained in our prior study ($E_g = 0.46$ eV).¹⁷ Within these limitations, we find that E_g monotonically increases with x from 0.19 eV for $x = 0.0$ to 0.23 eV for $x = 0.5$, to 0.34 eV for $x = 1.0$ and to 0.40 eV for $x = 1.5$.

Phase purity, chemical homogeneity and Se site preference. Figure 5 shows the XRPD pattern of the illustrative sample $\alpha\text{-As}_2\text{Te}_{2.6}\text{Se}_{0.4}$ (XRPD patterns for other compositions are given in the Supporting Information; Figures S1 to S4). In the $x = 0.0$ and 0.7 samples, weak additional reflections that can be attributed to either the cubic AsTe binary or elemental Te are observed. For the other compositions, all the reflections are indexed to the monoclinic $C2/m$ structure of $\alpha\text{-As}_2\text{Te}_3$, suggesting the absence of secondary phases within the detection limit of XRPD. SEM and EPMA confirmed the XRPD results except for $x = 1.0$ where some precipitates of elemental Te could be observed, the amount of which being below the detection limit of XRPD. Elemental X-ray maps reveal that all the elements are homogeneously distributed (Figures S5 to S11 in Supporting Information). The average chemical compositions obtained by EPMA (Table 1) indicate a good agreement between the nominal and actual compositions for all samples. The lattice parameters obtained from

Rietveld refinements are summarized in Table 1 and the reduced lattice parameters as well as the reduced unit cell volume are shown as a function of the Se content in Figure 6. These analyses indicate a monotonous shrinkage of the unit cell in a quasi-linear manner with increasing x due to the smaller covalent radius of Se with respect to Te. The overall decrease in the unit cell volume is accompanied by a slight variation in the monoclinic distortion associated with the β angle. The NPD pattern collected on the $x = 0.7$ sample (Figure 7) at 300 K provided further information on the distribution of Se on the three Te crystallographic sites of α -As₂Te₃. Rietveld refinements against these data were performed by considering three different structural models, where Se occupies one of the Te sites. The best agreement with the data was obtained when Se solely occupies the Te2 site, which is consistent with the predictions of the KKR-CPA calculations (see Tables S1 and S2 in the Supporting Information for the refined crystallographic parameters and main interatomic distances for the $x = 0.7$ sample).

Optical Band Gap. Figure 8a presents the Tauc-plot of the absorption spectra as a function of the photon energy E , assuming direct transitions for all samples. As shown in our previous study,¹⁷ the optical spectra of α -As₂Te₃ shows a steep rise above $E = 0.43$ eV attributed to the optical band gap E_g . This value is in good agreement with first-principles calculations of the electronic band structure of α -As₂Te₃.^{33,34} In the α -As_{2-x}Sn_xTe₃ series, all the optical spectra exhibited a shallow rise that was tentatively attributed to either impurity states in the band gap or intra-band scattering.¹⁷ Except for the end-member compounds α -As₂Te₃ and α -As₂Te_{1.5}Se_{1.5}, all the spectra display a similar shallow rise. This trend is followed by a steeper rise that likely corresponds to the band gap, the value of which first slightly decreases from 0.43 eV to 0.40 eV for $x = 0.1$, followed by a monotonous increase with increasing x up to 0.64 eV for $x = 1.5$ (Figure 8b). The overall increase in E_g with x is qualitatively in agreement with our band structure calculations. The tunability of E_g by substituting Se for Te can be

explained by the covalent radii of both atoms. The lower covalent radius of Se with respect to Te leads to a reduced orbital overlap and hence, to a decrease in the dispersion of the bands synonymous with an increase in E_g . The weak influence of isoelectronic Se on E_g from $x = 0.0$ to $x = 0.4$ is consistent with a nearly rigid-like evolution of the electronic band structure followed by a non-rigid-like behavior above $x = 0.4$.

Electronic and galvanomagnetic properties. In the following, only the data measured parallel to the pressing direction are shown for sake of clarity. The data measured perpendicular to the pressing direction are provided in the Supporting Information (Figures S12 to S14). Figure 9a shows the temperature dependence of the electrical resistivity ρ . For all samples, $\rho(T)$ decreases with increasing T indicative of their semiconducting nature. ρ decreases at 523 K from 650 $\mu\Omega\cdot\text{m}$ for $\alpha\text{-As}_2\text{Te}_3$ to 430 $\mu\Omega\cdot\text{m}$ for $\alpha\text{-As}_2\text{Te}_{2.6}\text{Se}_{0.4}$ before increasing by two orders of magnitude to reach 19000 $\mu\Omega\cdot\text{m}$ for $x = 1.5$. The initial decrease in the ρ values on going from $x = 0.0$ to $x = 0.4$ is most likely due to variations in the defect concentration that controls the transport in $\alpha\text{-As}_2\text{Te}_3$. The substitution of Se for Te tends to decrease their concentration and/or changing their nature. The significant increase in ρ observed above $x = 0.4$ is consistent with the optical absorption measurements and electronic band structure calculations, both of which indicating an increase in the band gap energy with x . As a result, the electronic band structure no longer evolves in a rigid-like manner above $x = 0.4$, explaining the lack of clear trend in $\rho(T)$ with x .

Figure 9b shows the thermopower α as a function of temperature for the series $\alpha\text{-As}_2\text{Te}_{3-x}\text{Se}_x$ measured parallel to the pressing direction. As in the Sn-substituted series,¹⁷ α appears isotropic to within experimental uncertainty (Figure S13 in Supporting Information). All samples show a p -type semiconducting behavior, indicating that the partial substitution of Se for Te does not lead to n -type conduction in the investigated compositional range. This lack of crossover can be attributed to the increase in the band gap values with increasing x .

The situation thus contrasts with Bi_2Te_3 where alloying with Se has a minimal impact on the band gap and favors the creation of Te_{Bi} antisite defects and Te vacancies, both of which being negatively charged.²⁰ $\alpha\text{-As}_2\text{Te}_3$ exhibits a maximum in α of $200 \mu\text{V K}^{-1}$ around 200 K, and is rapidly decreasing above this temperature up to around 500 K, where a transition from p - to n -type conduction is observed. This behavior was attributed to the prominent role played by defect chemistry in this compound.¹⁶ Alloying with Se up to $x = 0.4$ suppresses this dependence and yields a monotonous, non-linear increase in α with temperature. For $x \geq 0.7$, the maximum in α reached at high temperatures marks the onset of thermal excitations of minority carriers across the band gap that adversely affect the α values. The large α values that increase with increasing x are consistent with the semiconducting nature of the present samples.

The Hall carrier concentration p_{H} and the Hall mobility μ_{H} for the $\alpha\text{-As}_2\text{Te}_{3-x}\text{Se}_x$ samples are listed in Table 2. The results evidence a sudden increase in p_{H} from $3.4 \times 10^{18} \text{ cm}^{-3}$ for $x = 0.0$ to $2.4 \times 10^{19} \text{ cm}^{-3}$ for $x = 0.1$. This increase, similar to that observed in the Sn-substituted samples,¹⁷ is likely tied to variations in defect concentration upon Se alloying. Further increase in x results in a slight decrease in p_{H} down to $2.0 \times 10^{19} \text{ cm}^{-3}$ for $x = 0.4$, a value twice as high as those obtained in Sn-substituted samples. The presence of Se leads to very low hole mobilities, of the order of $1 \text{ cm}^2 \text{ V}^{-1} \text{ s}^{-1}$ as a result of alloy scattering, that is, an additional scattering mechanism introduced by the random distribution of Se atoms on the Te2 sites.

Thermal Transport Properties. Figures 10a and 10b show the temperature dependence of the total thermal conductivity κ for all samples. Note that the lower density of the samples with high Se contents has only a moderate influence on the measured values (estimated to at most 10% of the κ values for the $x = 1.5$ sample when considering the model developed by Landauer (Ref. 35) that takes into account the relative density of the samples). The measurements evidence a moderate anisotropy that tends to decrease with increasing x (Figure

S14 in Supporting Information), as already observed in Sn-substituted α -As₂Te₃.¹⁷ The high electrical resistivity of the samples results in negligible electronic contributions to the thermal conductivity. Hence, the measured κ values can be considered to reflect solely the lattice contribution in the temperature range where bipolar conduction is absent. For all samples, κ exhibits a well-defined Umklapp peak around 20 K, characteristic of crystalline solids. Above this temperature, κ decreases with increasing temperature, following roughly a T^{-1} law, indicative of thermal transport dominated by Umklapp scattering. Upon Se alloying, κ decreases up to $x = 1.5$, a behavior consistent with increased point-defect scattering expected in solid solutions. Regardless of the Se content, the room-temperature κ values are below 1 W m⁻¹ K⁻¹. Except for α -As₂Te₃ that experiences bipolar conduction above 450 K, κ decreases upon heating to reach ~ 0.35 W m⁻¹ K⁻¹ at 523 K in the $x = 1.5$ compound. This last value is the lowest achieved so far in both α - and β -As₂Te₃ compounds (Refs. 16 and 17) and among most of state-of-art thermoelectric selenide compounds.³⁶⁻³⁹ For α -As₂Te_{1.5}Se_{1.5}, κ is very close to the amorphous limit estimated to 0.4 W m⁻¹ K⁻¹ in these compounds and approaches the values measured in chalcogenide glasses of similar composition.¹⁷

As shown in Figure 11a, the decrease in κ with increasing disorder in the unit cell, *i.e.* with increasing x , follows the expectations of classical models for point-defect scattering of phonons. The lattice thermal conductivity of the alloyed compounds $\kappa_{L,A}$ was calculated by the model developed by Callaway and Klemens using the thermal conductivity of the pure end-member compounds, $\kappa_{L,P}$, and assuming that both Umklapp and point-defect scattering processes dominate^{40,41}

$$\frac{\kappa_{L,A}}{\kappa_{L,P}} = \frac{\arctan(u)}{u} \quad (1)$$

$$u^2 = \frac{\pi \cdot \theta_D \cdot \Omega}{2 \cdot h \cdot v^2} \kappa_{L,P} \Gamma \quad (2)$$

In Eqs.(1) and (2), Ω is the average volume per atom, θ_D is the Debye temperature, h is the Planck constant, v is the average speed of sound measured on the pure compounds and Γ is the scattering parameter defined as^{40,42-44}

$$\Gamma = \Gamma_{mass} + \Gamma_{strain\ field} = x(1 - x) \left[\left(\frac{\Delta M}{M_{avg}} \right)^2 + \varepsilon \left(\frac{\Delta \delta}{\delta_{avg}} \right)^2 \right] C \quad (3)$$

where x is the relative concentration of the impurity atom, M_{avg} and δ_{avg} are the average molar mass and atomic radius, respectively, ΔM and $\Delta \delta$ are the molar mass and atomic radius differences, respectively, between those of the substituting and substituted atoms. For a compound of chemical formula $A_m B_{n(1-x)} S_{nx}$ where B is substituted by the atoms S , the parameter C is defined as follows^{43,44}

$$C = \frac{n}{m + n} \frac{M_{avg}}{M_{tot}} \quad (4)$$

In Eq.(4), M_{tot} is the total molar mass as described in Ref. 43. Γ_{mass} corresponds to the scattering related to atomic mass contrast while $\Gamma_{strain\ field}$ describes the scattering due to the network distortion. In this model, ε is a phenomenological fitting parameter that can be related to the Grüneisen parameter characterizing the anharmonicity of the lattice vibrations.⁴¹ Typical values of ε fall within the range 10 – 100 for various thermoelectric materials.⁴¹ Taking the covalent radii of the atoms for the parameter δ , this model was used to calculate the blue curve shown in Figure 11a yielding a fit ε value of 12, that is, in the above-mentioned range. The good agreement achieved with the experimental results indicates that the decrease in κ with increasing the Se content can be attributed to enhanced point-defect scattering.

Figure 11b shows the ratio between Γ_{mass} and $\Gamma_{strain\ field}$ as a function of the Se content. While Γ increases with x , the ratio $\Gamma_{strain\ field} / \Gamma_{mass}$ linearly decreases with increasing the Se content. At low substitution levels, phonon scattering due to mass fluctuations is the dominant term, while at higher Se contents up to $x = 1.5$, the relative influence of both effects balances.

However, the variations in strain field fluctuations relative to mass fluctuations is not straightforward, as not only does it depend on the atom mass differences with respect to the atomic radii differences, but also on the bonding character and crystallographic site environment.⁴⁵ In particular, the site preference of Se leads to an inhomogeneous distribution of Se atoms within the unit cell, the variation of which with x implying an evolution in strain field fluctuations.

Dimensionless thermoelectric figure of merit ZT . The temperature dependence of the ZT values is shown in Figure 12. The mixed electrical conduction of the binary compound above 200 K leads to very low ZT values. The ZT values increase with x up to $x = 0.4$ due to the concomitant decrease in ρ and increase in α to reach maximum of 0.17 at 523 K. Above $x = 0.4$, this trend reverses and the ZT values decrease with increasing x due to the large electrical resistivity values. Hence, Se alloying has an overall detrimental effect on the electrical properties and does not enable achieving higher thermoelectric performances compared to substitutions of Sn and Bi for As.^{17,19}

Summary and conclusion

The solid solution α -As₂Te_{3-x}Se_x ($0 \leq x \leq 1.5$) has been successfully synthesized by a combination of powder metallurgy and spark plasma sintering. The monoclinic crystal structure of α -As₂Te₃ is preserved across the Se concentration range studied. As suggested by room-temperature NPD data and KKR-CPA calculations, Se preferentially occupies the Te2 site due to the weaker modifications of the electronic band structure induced by this substitution. Calculations further indicate a rigid-like behavior at low Se contents, a prediction in agreement with the nearly constant optical band gap measured between $x = 0.0$ and $x = 0.4$ and band gap opening at higher substitution levels. Unlike the solid solution Bi₂Te_{3-x}Se_x,

where substituting Se for Te leads to a *n*-type behavior, this substitution leaves unchanged the *p*-type electrical conduction of α -As₂Te₃. The samples show semiconducting-like properties with large electrical resistivity and thermopower values that increase with increasing *x*. Despite the very low lattice thermal conductivity values measured in α -As₂Te₃ (0.5 W m⁻¹ K⁻¹ above 300 K), Se substitution further lowers the lattice contribution that reaches an extremely low value of 0.35 W m⁻¹ K⁻¹ above 300 K in α -As₂Te_{1.5}Se_{1.5}. This reduction is due to increased disorder in the unit cell upon alloying with Se, the influence of which on the lattice thermal conductivity is well described by classical models for alloy scattering of phonons.

Associated Content

The Supporting Information is available free of charge on the ACS Publications website.

Rietveld refinements of the XRPD patterns of the *x* = 0.0, 0.1, 0.2 and 0.7 samples; Backscattered electron images and elemental X-ray mappings of the α -As₂Te_{3-*x*}Se_{*x*} samples; Tables S1 and S2; Temperature dependence of the electrical resistivity, thermopower and total thermal conductivity measured perpendicular to the pressing direction. (PDF)

Author Information

+ Present Address: *National Institute for Materials Science (NIMS), 1 Chome-2-1 Sengen, Tsukuba, Ibaraki 305-0047, Japan*

Corresponding Author

*E-mail: bertrand.lenoir@univ-lorraine.fr

Notes

The authors declare no competing financial interest.

Acknowledgments

The authors would like to thank financial support from the French National Agency (ANR) in the frame of its programme "PROGELEC" (Verre Thermo-Générateur "VTG"). B.W. and J.T. were partly supported by the National Science Center (Poland) (Project No. DEC-2011/02/A/ST3/00124). J.-B. V. and B. L. thank P. Boulet for his help in the measurement of the XRPD pattern of $P2_1/n$ As_2Se_3 . The authors thank the Institut Laue Langevin (ILL) for granting access to the D1B neutron scattering instrument.

Tables

Table 1. Nominal and actual compositions obtained by EPMA and lattice parameters determined by Rietveld refinements against the XRPD data of the series α -As₂Te_{3-x}Se_x. All the compositions were normalized to five atoms per chemical formula.

<i>Nominal composition</i>	<i>EPMA</i>	<i>a</i> (Å)	<i>b</i> (Å)	<i>c</i> (Å)	<i>β</i> (°)
As ₂ Te ₃	As _{1.985} Te _{3.015}	14.3392(4)	4.0146(1)	9.8859(3)	95.046(1)
As ₂ Te _{2.9} Se _{0.1}	As _{1.993} Te _{2.919} Se _{0.087}	14.3302(7)	4.0074(2)	9.8740(5)	95.029(2)
As ₂ Te _{2.8} Se _{0.2}	As _{2.001} Te _{2.812} Se _{0.187}	14.3184(7)	3.9955(2)	9.8511(5)	94.940(2)
As ₂ Te _{2.6} Se _{0.4}	As _{2.010} Te _{2.635} Se _{0.355}	14.3010(7)	3.9812(2)	9.8253(4)	94.860(2)
As ₂ Te _{2.4} Se _{0.7}	As _{2.052} Te _{2.277} Se _{0.671}	14.2745(6)	3.9515(1)	9.7564(4)	94.651(1)
As ₂ Te ₂ Se ₁	As _{2.026} Te _{1.879} Se _{1.096}	14.2073(2)	3.9171(4)	9.6785(1)	94.595(5)
As ₂ Te _{1.5} Se _{1.5}	As _{2.097} Te _{1.436} Se _{1.467}	14.126(2)	3.8825(4)	9.6161(2)	94.561(5)

Table 2. Electrical resistivity ρ , hole concentration p_H and Hall mobility μ_H at 300 K of α -As₂Te_{3-x}Se_x for $x = 0.0, 0.1, 0.2$ and 0.4 . Because the binary α -As₂Te₃ features a mixed electrical conduction above 250 K, the Hall carrier concentration inferred at 300 K should be taken as an upper limit to the actual value while the Hall mobility should be considered as a lower limit.

<i>Nominal composition</i>	ρ ($\mu\Omega$ m)	p_H (cm ⁻³)	μ_H (cm ² V ⁻¹ s ⁻¹)
As ₂ Te ₃	5500	3.4×10^{18}	3.3
As ₂ Te _{2.9} Se _{0.1}	2000	2.4×10^{19}	1.3
As ₂ Te _{2.8} Se _{0.2}	1500	2.3×10^{19}	1.8
As ₂ Te _{2.6} Se _{0.4}	1700	2.0×10^{19}	1.8

Figures captions

Figure 1. Crystal structure of α -As₂Te₃ (space group $C2/m$). The As and Te atoms are shown in black and white, respectively. As atoms occupy the As1 ($4i, (x, 0.5, z)$) and As2 ($4i, (x, 0, z)$) sites while Te atoms are located on three distinct sites labelled Te1 ($4i, (x, 0, z)$), Te2 ($4i, (x, 0.5, z)$) and Te3 ($4i, (x, 0, z)$).

Figure 2. Energy dependence of the total and site-decomposed density of states (DOS) of α -As₂Te_{2.5}Se_{0.5} with Se located on the Te1 (upper panel), Te2 (middle panel) or Te3 (lower panel) site. In all panels, the Fermi level has been arbitrarily placed at 0 eV.

Figure 3. Energy dependence of the total and site-decomposed density of states (DOS) of α -As₂Te₂Se with Se located on either the Te2 (upper panel) or Te3 (lower panel) site. In both panels, the Fermi level has been arbitrarily placed at 0 eV.

Figure 4. Energy dependence of the total and site-decomposed density of states (DOS) of α -As₂Te_{1.5}Se_{1.5} with Se occupying either the Te1 and Te2 sites (upper panel) or the Te2 and Te3 sites (lower panel). In both panels, the Fermi level has been arbitrarily placed at 0 eV.

Figure 5. Experimental XRPD pattern (black curve) and calculated profile (red curve) for the composition α -As₂Te_{2.6}Se_{0.4}. The positions of the Bragg reflections are marked by vertical red bars and the difference between the experimental and calculated profile is shown by the solid blue curve.

Figure 6. Reduced lattice parameters a/a_0 , b/b_0 , c/c_0 and reduced unit cell volume V/V_0 as a function of the Se content x . The solid lines are guide to the eye. a_0 , b_0 , c_0 , β_0 and V_0 correspond to the values of the unsubstituted compound α -As₂Te₃ (see Table 1).

Figure 7. Rietveld analysis of the experimental neutron powder diffraction pattern for α -As₂Te_{2.3}Se_{0.7} at 300 K. The open red circles are the experimental data, the solid black line is the calculated pattern, the bottom blue line is the difference between the experimental and theoretical patterns and the green vertical ticks stand for the Bragg reflections of α -As₂Te_{2.3}Se_{0.7}. The reliability factors are $R_{wp} = 4.5\%$ and $R_B = 6.2\%$.

Figure 8. (a) Optical absorption spectra of α -As₂Te_{3-x}Se_x for $x = 0.0, 0.1, 0.2, 0.4, 0.7, 1.0$ and 1.5 . The intersection of the solid black lines with the x -axis provides an estimation of the optical band gap. (b) Comparison of the experimental and theoretical evolution of the optical band gap E_g with x .

Figure 9. (a) Temperature dependence of the electrical resistivity ρ and (b) thermopower α for the α -As₂Te_{3-x}Se_x solid solution with $x = 0.0, 0.1, 0.2, 0.4, 0.7, 1.0$ and 1.5 . In both panels, only the values measured parallel to the pressing direction are shown. The color-coded symbols are similar in both panels. The lack of α data for the $x = 1.5$ sample below 200 K is due to the too large electrical resistivity values that prevent α from being measured.

Figure 10. Total thermal conductivity κ as a function of temperature for the solid solution α -As₂Te_{3-x}Se_x at low (a) and high temperatures (b) for $x = 0.0, 0.1, 0.2, 0.4, 0.7, 1.0$ and 1.5 . The two data sets are separated for sake of clarity. The difference observed at 300 K between the values measured at low and high temperatures is due to thermal radiations inherent to the measurement technique used at low temperatures. The color-coded symbols are similar in both panels. Considering the rather high electrical resistivity values of all samples, the total thermal conductivity can be considered to reflect exclusively the lattice contribution κ_L .

Figure 11. (a) Thermal conductivity averaged on all direction at 300 K as a function of the Se content for the solid solution α -As₂Te_{3-x}Se_x. (b) Calculated ratios of the scattering effect constant relative to strain field fluctuations and mass contrast as a function of x .

Figure 12. Temperature dependence of the dimensionless thermoelectric figure of merit ZT for α -As₂Te_{3-x}Se_x with $x = 0.0, 0.1, 0.2, 0.4, 0.7, 1.0$ and 1.5 .

References

- (1) *Thermoelectrics and Its Energy Harvesting*; Rowe, D. M., Ed.; CRC Press: Boca Raton, FL, 2012.
- (2) Goldsmid, H. J. In *Thermoelectric Refrigeration*; Temple Press Books Ltd: London, U.K., 1964.
- (3) Poudel, B.; Hao, Q.; Ma, Y.; Lan, Y.; Minnich, A.; Yu, B.; Yan, X.; Wang, D.; Muto, A.; Vashaee, D.; Chen, X.; Liu, J.; Dresselhaus, M. S.; Chen, G.; Ren, Z. High-thermoelectric performance of nanostructured bismuth antimony telluride bulk alloys. *Science* **2008**, *320*, 634 – 638.
- (4) Jaworski, C. M.; Kulbachinskii, V.; Heremans, J. P. Resonant level formed by tin in Bi_2Te_3 and the enhancement of room-temperature thermoelectric power. *Phys. Rev. B: Condens. Matter Mater. Phys.* **2009**, *80*, 233201.
- (5) Xie, W.; He, J.; Jung Kang, H.; Tang, X.; Zhu, S.; Laver, M.; Wang, S.; Copley, J. R. D.; Brown, C. M.; Zhang, Q.; Tritt, T. M. Identifying the specific nanostructures responsible for the high thermoelectric performance of $(\text{Bi,Sb})_2\text{Te}_3$ nanocomposites. *Nano Lett.* **2010**, *10*, 3283 – 3289.
- (6) Kim, S. I.; Lee, K. H.; Mun, H. A.; Kim, H. S.; Hwang, S. W.; Roh, J. W.; Yang, D. J.; Shin, W. H.; Li, X. S.; Lee, Y. H.; Snyder, G. J.; Kim, S. W. Dense dislocation arrays embedded in grain boundaries for high-performance bulk thermoelectrics. *Science* **2015**, *348*, 109 – 114.
- (7) Vaney, J. B.; Delaizir, G.; Alleno, E.; Rouleau, O.; Piarristeguy, A.; Monnier, J.; Godart, C.; Ribes, M.; Escalier, R.; Pradel, A. Gonçalves, A. P.; Cuello, G. J.; Ziolkowski, P.; Müller, E.; Candolfi, C.; Dauscher, A.; Lenoir, B. A comprehensive study of the crystallization of

Cu–As–Te glasses: microstructure and thermoelectric properties. *J. Mater. Chem. A* **2013**, *1*, 8190 – 8200.

(8) Yakushev, V. G.; Kirinsky, V. A. New polymorphic modification of arsenic telluride, produced at high pressures. *Doklady Akad Nauk SSSR*. **1969**, 882 – 884.

(9) Toscani, S.; Dugué, J.; Ollitrault, R.; Céolin, R. Polymorphism of As₂Te₃: structural studies and thermal behaviour of rhombohedral β-As₂Te₃. *Thermochim. Acta* **1991**, *186*, 247 – 251.

(10) Zhao, J.; Yang, L.; Yu, Z.; Wang, Y.; Li, C.; Yang, K.; Liu, Z.; Wang, L. Structural phase transitions and metallized phenomena in arsenic telluride under high pressure. *Inorg. Chem.* **2016**, *55*, 3907 – 3914.

(11) Zhang, Y.; Ma, Y.; Geng, A.; Zhu, C.; Liu, G.; Tao, Q.; Li, F.; Wang, Q.; Li, Y.; Wang, X.; Zhu, P. Pressure-induced electronic phase transitions of α-As₂Te₃. *J. Alloys Compd.* **2016**, *685*, 551 – 558.

(12) Cuenca-Gotor, V. P.; Sans, J. A.; Ibanez, J.; Popescu, C.; Gomis, O.; Vilaplana, R.; Manjon, F. J.; Leonardo, A.; Sagasta, E.; Suarez-Alcubilla, A.; Gurtubay, I. G.; Mollar, M.; Bergara, A. Structural, vibrational, and electronic study of α-As₂Te₃ under compression. *J. Phys. Chem. C* **2016**, *120*, 19340 – 19352.

(13) Morin, C.; Corallini, S.; Carreaud, J.; Vaney, J.-B.; Delaizir, G.; Crivello, J.-C.; Lopes, E. B.; Piarristeguy, A.; Monnier, J.; Candolfi, C.; Nassif, V.; Cuello, G. J.; Pradel, A.; Gonçalves, A. P.; Lenoir, B.; Alleno, E. Polymorphism in thermoelectric As₂Te₃. *Inorg. Chem.*, **2015**, *54*, 9936 – 9947.

(14) Harman, T. C.; Paris, B.; Miller, S. E.; Goering, H. L. Preparation and some physical properties of Bi₂Te₃, Sb₂Te₃ and As₂Te₃. *J. Phys. Chem. Solids*, **1957**, *2*, 181 – 190.

(15) Carron, G. J. The crystal structure and powder data for arsenic telluride. *Acta Cryst.* **1963**, *16*, 338 – 343.

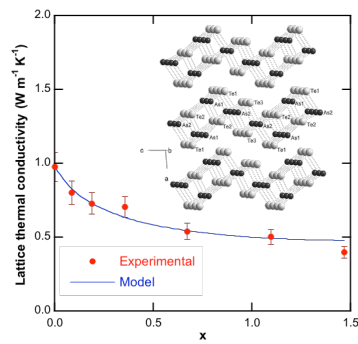
- (16) Vaney, J. B.; Carreaud, J.; Delaizir, G.; Morin, C.; Monnier, J.; Alleno, E.; Piarristeguy, A.; Pradel, A.; Gonçalves, A. P.; Lopes, E. B.; Candolfi, C.; Dauscher, A.; Lenoir, B. Thermoelectric properties of the α -As₂Te₃ crystalline phase. *J. Electron. Mater.* **2016**, *45*, 1447 – 1452.
- (17) Vaney, J. B.; Carreaud, J.; Delaizir, G.; Piarristeguy, A.; Pradel, A.; Alleno, E.; Monnier, J.; Lopes, E. B.; Gonçalves, A. P.; Dauscher, A.; Candolfi, C.; Lenoir, B. High thermoelectric performance in Sn-substituted α -As₂Te₃. *J. Mater. Chem. C*, **2016**, *4*, 2329 – 2338.
- (18) Vaney, J. B.; Carreaud, J.; Delaizir, G.; Pradel, A.; Piarristeguy, A.; Morin, C.; Alleno, E.; Monnier, J.; Gonçalves, A. P.; Candolfi, C.; Dauscher, A.; Lenoir, B. High-temperature thermoelectric properties of Sn-doped β -As₂Te₃. *Adv. Electron. Mater.* **2015**, *1*, 1400008.
- (19) Vaney, J. B.; Delaizir, G.; Piarristeguy, A.; Monnier, J.; Alleno, E.; Lopes, E. B.; Gonçalves, A. P.; Pradel, A.; Dauscher, A.; Candolfi, C.; Lenoir, B. High-temperature thermoelectric properties of the β -As_{2-x}Bi_xTe₃ solid solution. *APL Mater.* **2016**, *4*, 104901.
- (20) Horák, J.; Star, Z.; Votinsk, J. Point defects in the mixed chalcogenides Bi₂Te_{3-x}X_x (X= S, Se). *Philos. Mag. B* **1994**, *69*, 31 – 38.
- (21) Champness, C.; Muir, W.; Chiang, P. Thermoelectric properties of *n*-type Bi₂Te₃–Bi₂Se₃ alloys. *Can. J. Phys.* **1967**, *45*, 3611 – 3626.
- (22) Misra, S.; Bever, M. B. On the solid solutions of bismuth telluride and bismuth selenide. *J. Phys. Chem. Solids* **1964**, *25*, 1233 – 1241.
- (23) Miller, G. R.; Li, C. Y.; Spencer, C. W. Properties of Bi₂Te₃-Bi₂Se₃ alloys. *J. Appl. Phys.* **1963**, *34*, 1398 – 1400.
- (24) Kirkinsky, V.; Ryaposov, A.; Yakushev, V. Synthesis of third polymorphic modification of selenide arsenic at high pressures. *Fiz. Tverd. Tela* **1969**, *11*, 2382 – 2384.
- (25) Stergiou, A.; Rentzeperis, P. The crystal structure of arsenide selenide As₂Se₃. *Z. Kristallog.* **1985**, *173*, 185 – 192.

- (26) Rodriguez-Carvajal, J. Recent advances in magnetic structure determination by neutron powder diffraction. *Physica* **1993**, *192*, 55 – 69.
- (27) Alleno, E.; Bérardan, D.; Byl, C.; Candolfi, C.; Daou, R.; Decourt, R.; Guilmeau, E.; Hébert, S.; Hejtmanek, J.; Lenoir, B.; Masschelein, P.; Ohorodniichuk, V.; Pollet, M.; Populoh, S.; Ravot, D.; Rouleau, O.; Soulier, M. A round robin test of the uncertainty on the measurement of the thermoelectric dimensionless figure of merit of $\text{Co}_{0.97}\text{Ni}_{0.03}\text{Sb}_3$. *Rev. Sci. Instrum.* **2015**, *86*, 011301.
- (28) Kubelka, P.; Monk, F. Ein Beitrag zur Optik der Farbanstriche. *Z. Tech. Phys.* **1931**, *12*, 593 – 601.
- (29) Bansil, A.; Kaprzyk, S.; Mijnaerends, P. E.; Tobola, J. Electronic structure and magnetism of $\text{Fe}_{3-x}\text{V}_x\text{X}$ ($X = \text{Si}, \text{Ga}, \text{and Al}$) alloys by the KKR-CPA method. *Phys. Rev. B: Condens. Matter Mater. Phys.* **1999**, *60*, 13396 – 13412.
- (30) Stopa, T.; Kaprzyk, S.; Tobola, J. Linear aspects of the Korringa–Kohn–Rostoker formalism. *J. Phys.: Condens. Matter* **2004**, *16*, 4921 – 4933.
- (31) Perdew, J. P.; Wang, Y. Accurate and simple analytic representation of the electron-gas correlation energy. *Phys. Rev. B: Condens. Matter Mater. Phys.* **1992**, *45*, 13244 – 13249.
- (32) Kaprzyk S.; Bansil, A. Green's function and a generalized Lloyd formula for the density of states in disordered muffin-tin alloys. *Phys. Rev. B: Condens. Matter Mater. Phys.* **1990**, *42*, 7358 – 7362.
- (33) Sharma, Y.; Srivastava, P. First principles investigation of electronic, optical and transport properties of α - and β -phase of arsenic telluride. *Opt. Mater.* **2011**, *33*, 899 – 904.
- (34) Vaney, J. B.; Crivello, J.-C.; Morin, C.; Delaizir, G.; Carreaud, J.; Piarristeguy, A.; Monnier, J.; Alleno, E.; Pradel, A.; Lopes, E. B.; Gonçalves, A. P.; Dauscher, A.; Candolfi, C.; Lenoir, B. Electronic structure, low-temperature transport and thermodynamic properties of polymorphic β - As_2Te_3 . *RSC Adv.* **2016**, *6*, 52048 – 52057.

- (35) Landauer, R. The electrical resistance of binary metallic mixtures. *J. Appl. Phys.* **1952**, *23*, 779.
- (36) Chen, C.-L.; Wang, H.; Chen, Y.-Y.; Day, T.; Snyder, G. J. Thermoelectric properties of *p*-type polycrystalline SnSe doped with Ag. *J. Mater. Chem. A* **2014**, *2*, 11171 – 11176.
- (37) Sassi, S.; Candolfi, C.; Vaney, J.-B.; Ohorodniichuk, V.; Masschelein, P.; Dauscher, A.; Lenoir, B. Assessment of the thermoelectric performance of polycrystalline *p*-type SnSe. *Appl. Phys. Lett.* **2014**, *104*, 212105.
- (38) Wei, T.-R.; Wu, C.-F.; Zhang, X.; Tan, Q.; Sun, L.; Pan, Y.; Li, J.-F. Thermoelectric transport properties of pristine and Na-doped SnSe_{1-x}Te_x polycrystals. *Phys. Chem. Chem. Phys.* **2015**, *17*, 30102 – 30109.
- (39) Lee, Y.; Lo, S.-H.; Androulakis, J.; Wu, C.-I.; Zhao, L.-D.; Chung, D.-Y.; Hogan, T. P.; Dravid, V. P.; Kanatzidis, M. G. High-performance tellurium-free thermoelectrics: all-scale hierarchical structuring of *p*-type PbSe–MSe systems (*M* = Ca, Sr, Ba). *J. Am. Chem. Soc.* **2013**, *135*, 5152 – 5160.
- (40) Callaway, J.; von Baeyer, H. C. Effect of point imperfections on lattice thermal conductivity. *Phys. Rev.* **1960**, *120*, 1149 – 1154.
- (41) Klemens, P. G. Thermal resistance due to point defects at high temperatures. *Phys. Rev.* **1960**, *119*, 507 – 509.
- (42) Abeles, B. Lattice thermal conductivity of disordered semiconductor alloys at high temperatures. *Phys. Rev.* **1963**, *131*, 1906 – 1911.
- (43) Slack, G. A. Thermal conductivity of MgO, Al₂O₃, MgAl₂O₄, and Fe₃O₄ crystals from 3° to 300°K. *Phys. Rev.* **1962**, *126*, 427 – 441.
- (44) Meisner, G. P.; Morelli, D. T.; Hu, S.; Yang, J.; Uher, C. Structure and lattice thermal conductivity of fractionally filled skutterudites: solid solutions of fully filled and unfilled end members. *Phys. Rev. Lett.* **1998**, *80*, 3551 – 3554.

(45) Yang, J.; Meisner, G. P.; Chen, L. Strain field fluctuation effects on lattice thermal conductivity of ZrNiSn-based thermoelectric compounds. *Appl. Phys. Lett.* **2004**, *85*, 1140 – 1142.

For Table of Contents Only



The solid solution $\alpha\text{-As}_2\text{Te}_{3-x}\text{Se}_x$ ($0 \leq x \leq 1.5$) has been synthesized and its structural and transport properties determined. Se substitution results in increased electrical resistivity and thermopower due to larger energy band gap and lowered lattice thermal conductivity due to enhanced point defect scattering.

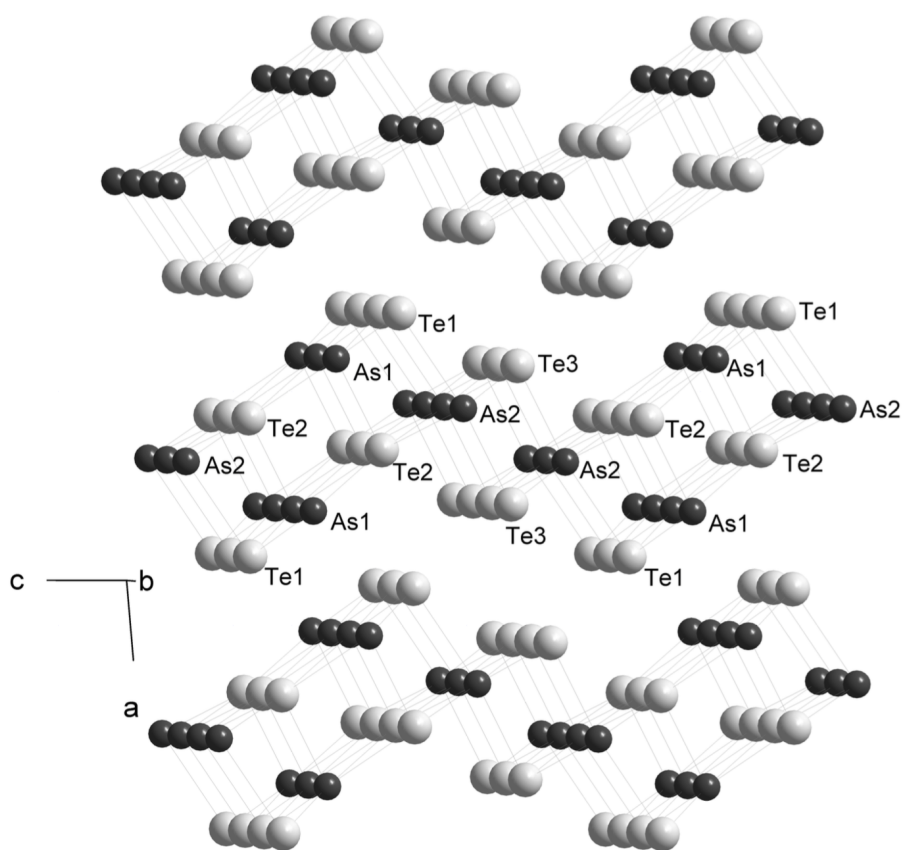


Figure 1

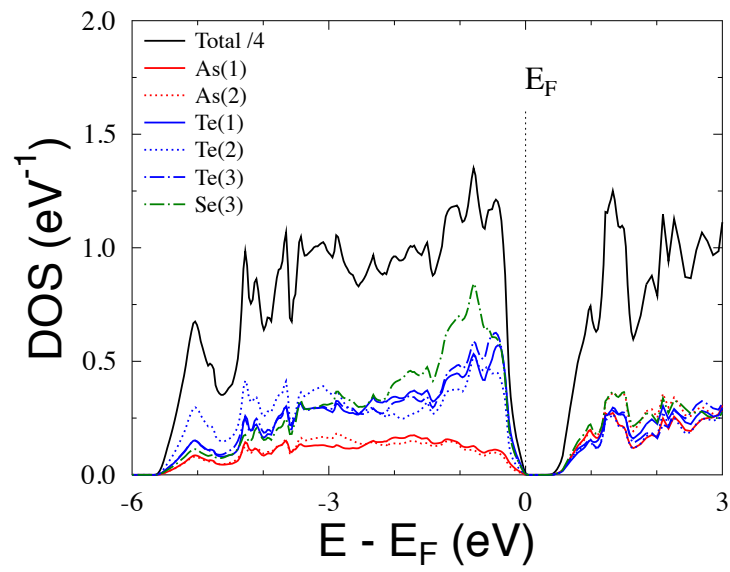
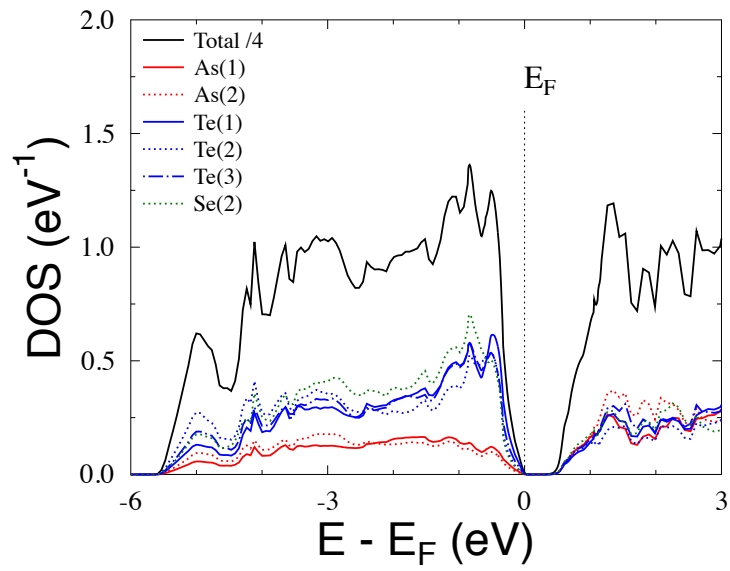
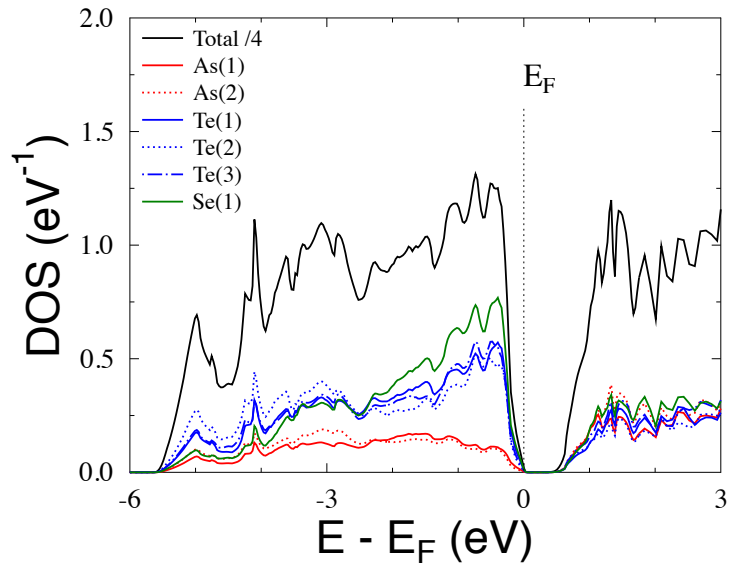


Figure 2

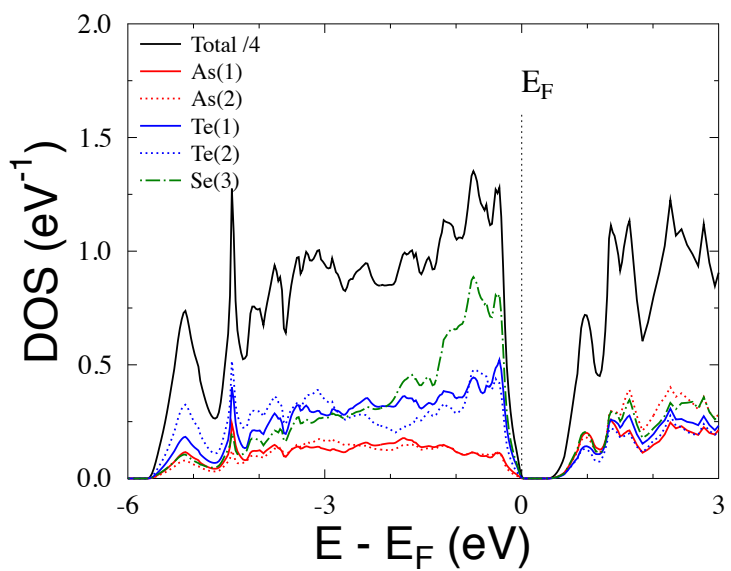
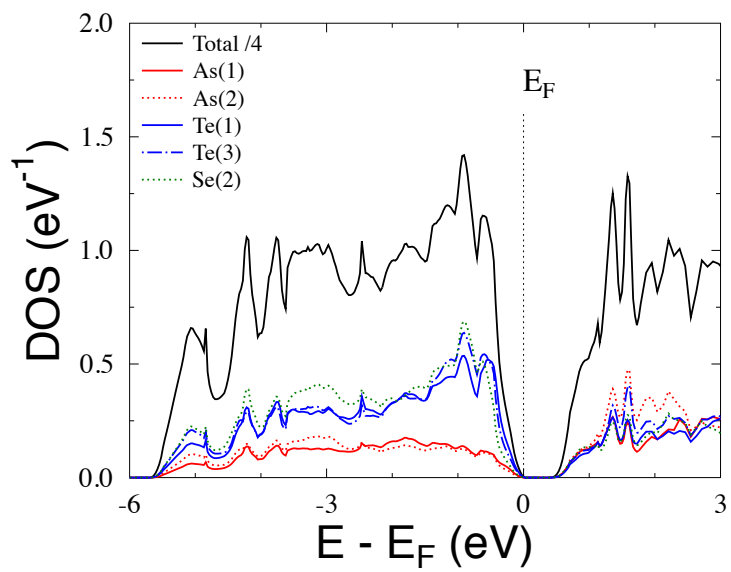


Figure 3

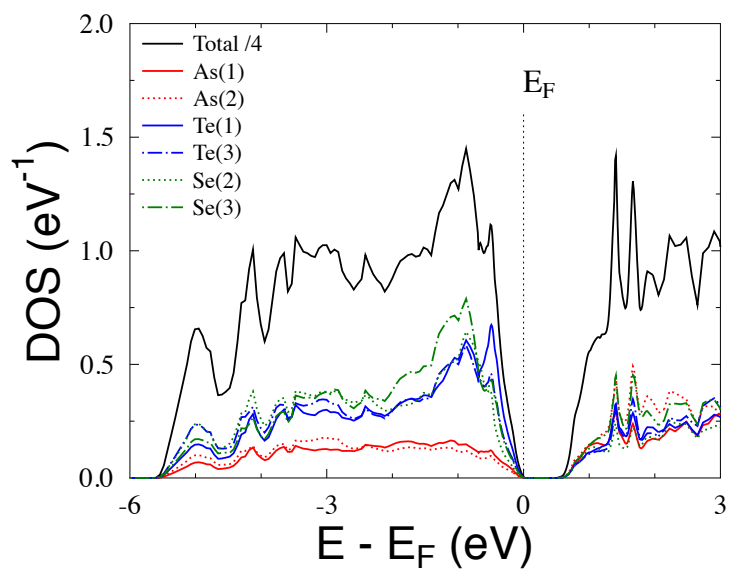
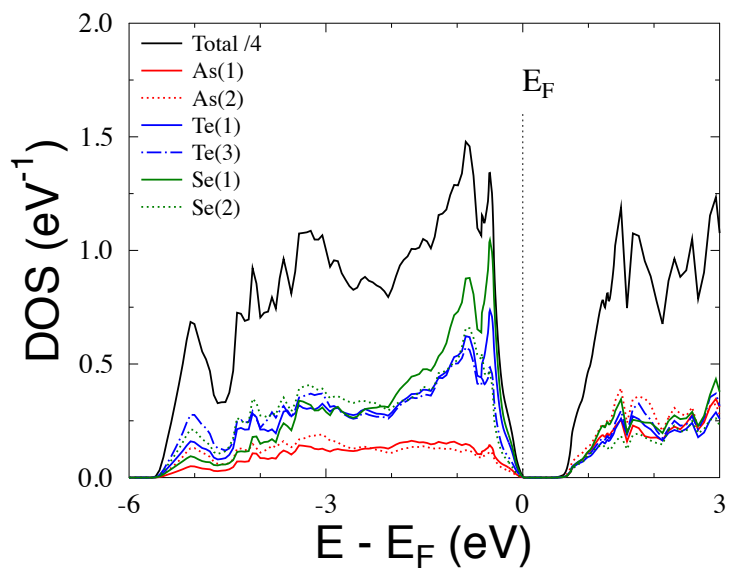


Figure 4

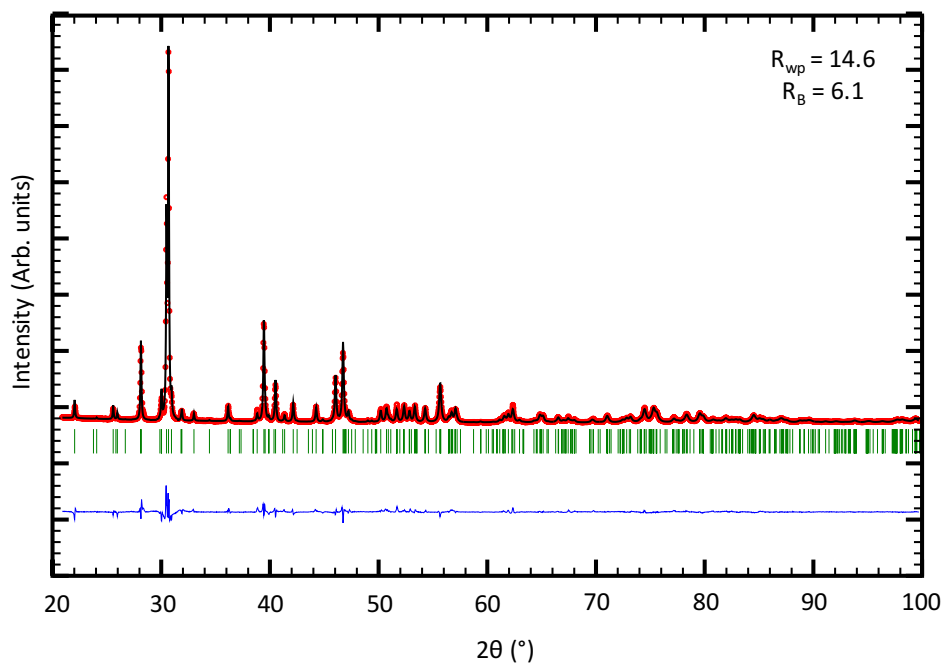


Figure 5

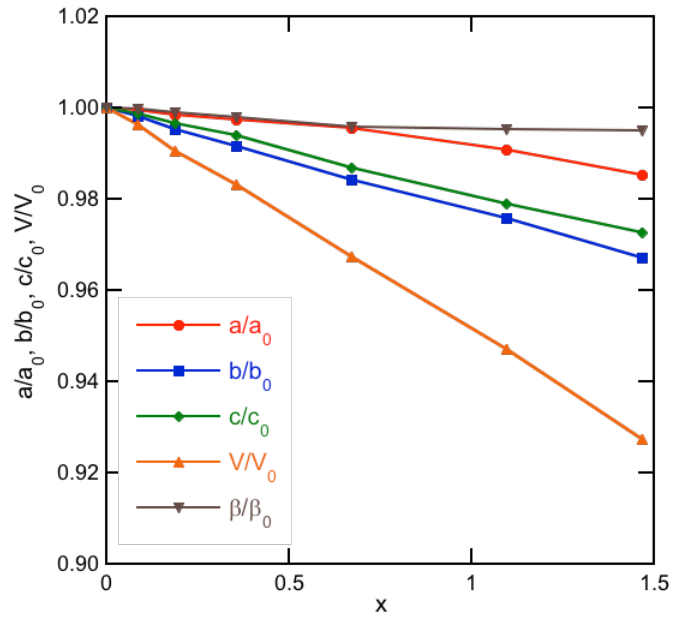


Figure 6

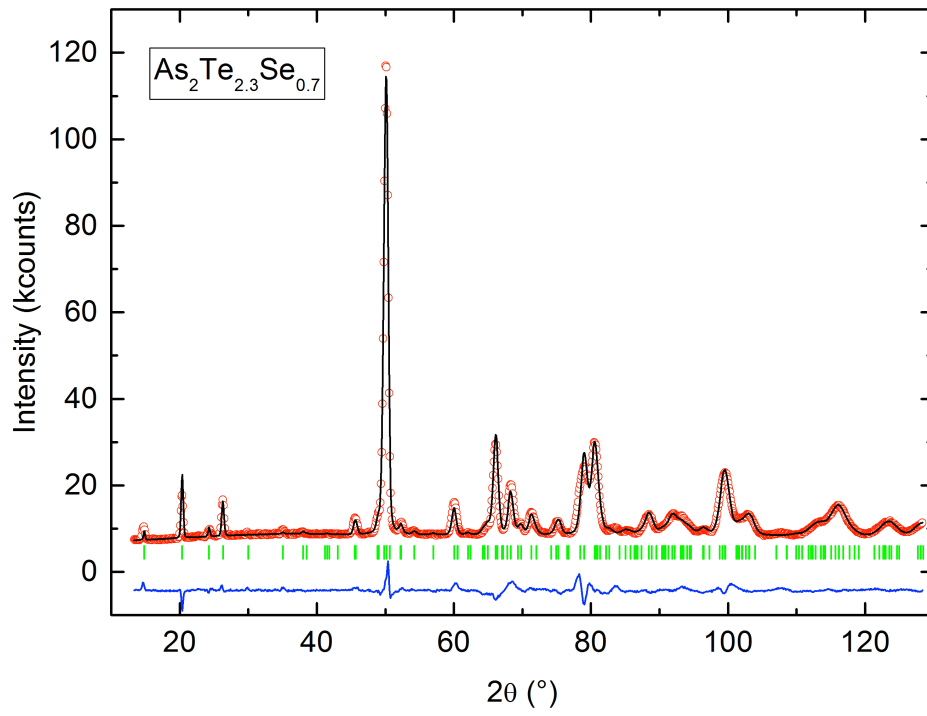


Figure 7

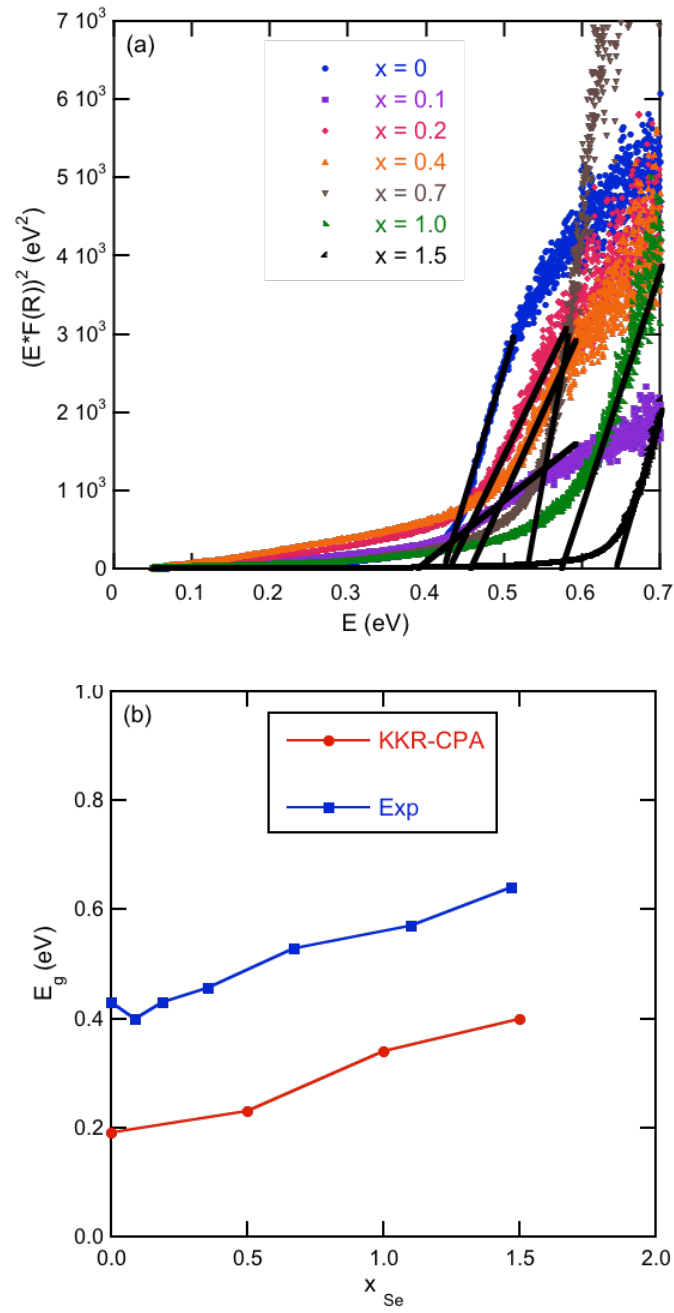


Figure 8

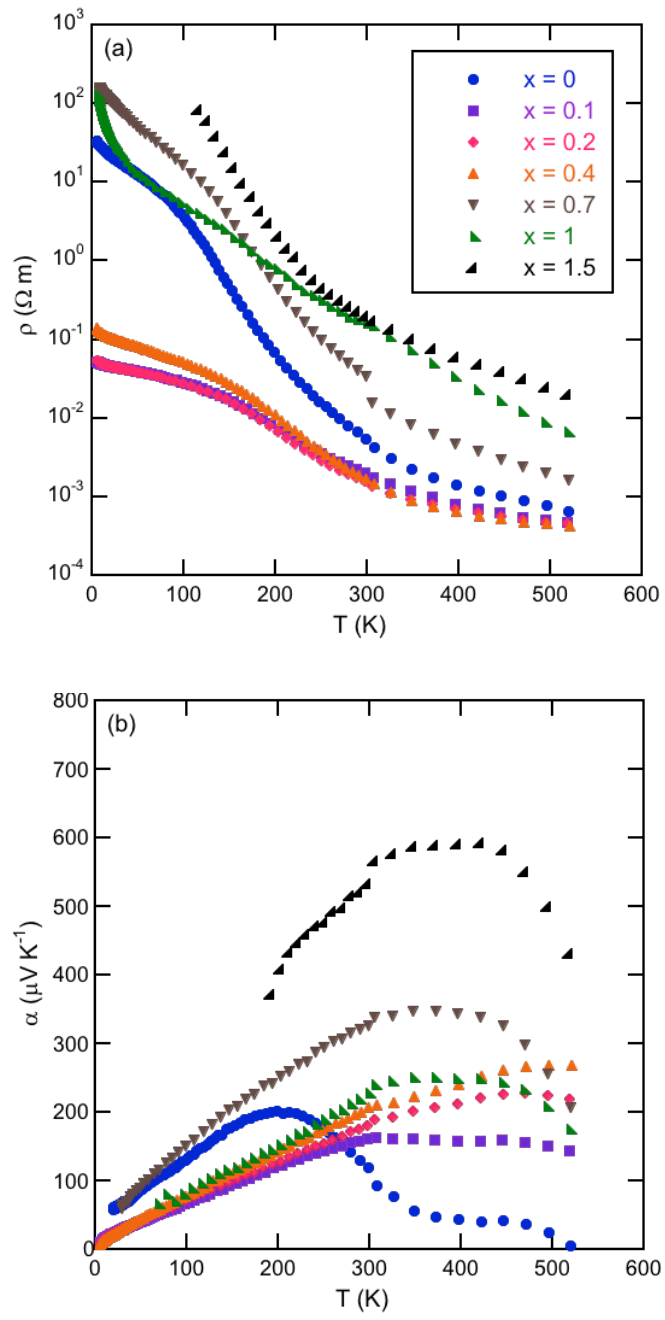


Figure 9

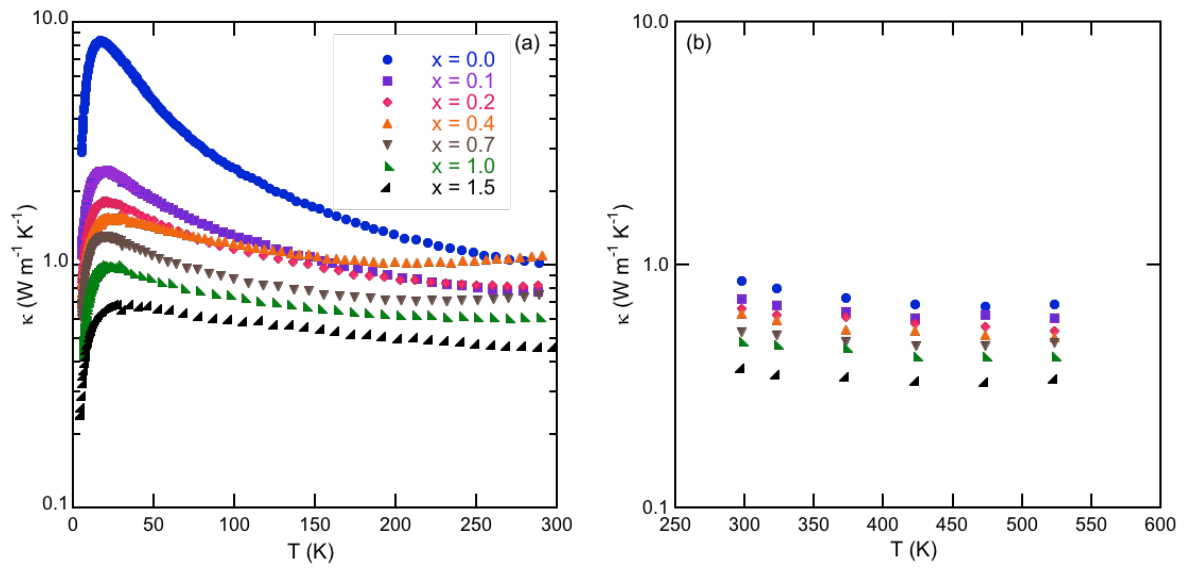


Figure 10

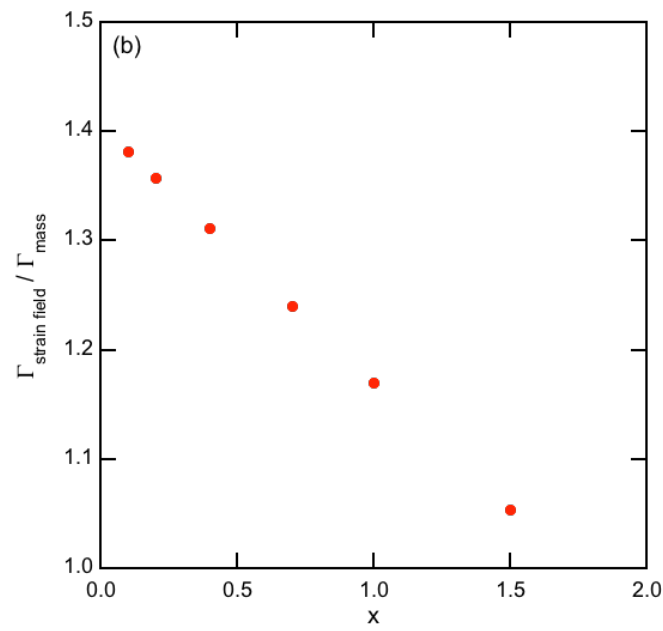
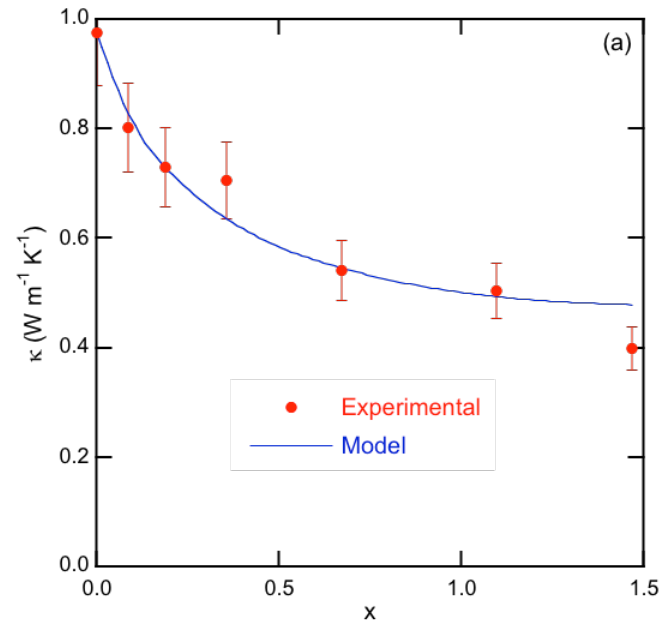


Figure 11

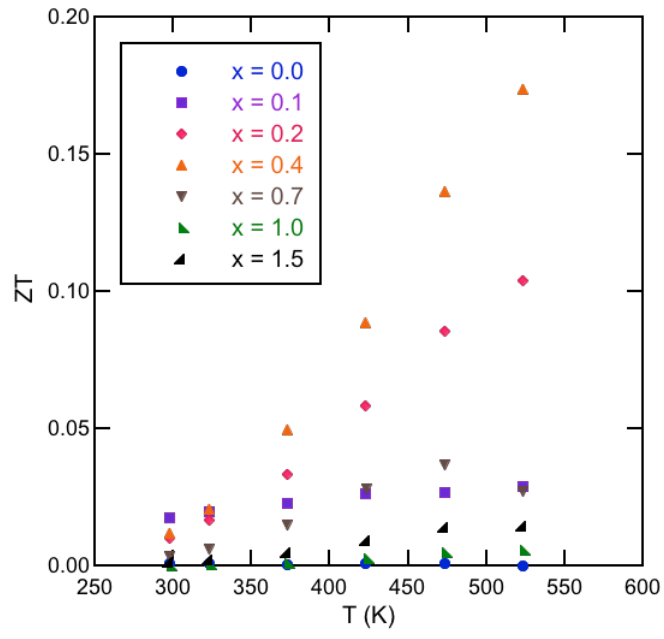


Figure 12